Article

Chemoenzymatic Syntheses of Fluorine-18-Labeled Disaccharides from [18F] FDG Yield Potent Sensors of Living Bacteria *In Vivo*

Alexandre M. Sorlin, Marina López-Álvarez, Sarah J. Rabbitt, Aryn A. Alanizi, Rebecca Shuere, Kondapa Naidu Bobba, Joseph Blecha, Sasank Sakhamuri, Michael J. Evans, Kenneth W. Bayles, Robert R. Flavell, Oren S. Rosenberg, Renuka Sriram, Tom Desmet, Bernd Nidetzky, Joanne Engel, Michael A. Ohliger, James S. Fraser, and David M. Wilson*

Cite This: https://doi.org/10.1021/jacs.3c03338

Read Online

ACCESS | Metrics & More | Article Recommendations | Supporting Information

ABSTRACT: Chemoenzymatic techniques have been applied extensively to pharmaceutical development, most effectively when routine synthetic methods fail. The regioselective and stereoselective construction of structurally complex glycans is an elegant application of this approach that is seldom applied to positron emission tomography (PET) tracers. We sought a method to dimerize 2-deoxy-[18F]-fluoro-D-glucose ([18F]FDG), the most common tracer used in clinical imaging, to form [18F]-labeled disaccharides for detecting microorganisms *in vivo* based on their bacteria-specific glycan incorporation. When [18F]FDG was reacted with β-D-glucose-1-phosphate in the presence of maltose phosphorylase, the α-1,4- and α-1,3-linked products 2-deoxy-[18F]-fluoro-maltose ([18F]FDM) and 2-deoxy-2-[18F]-fluoro-sakebiose

([18F]FSK) were obtained. This method was further extended with the use of trehalose (α,α-1,1), laminaribiose (β-1,3), and cellobiose (β-1,4) phosphorylases to synthesize 2-deoxy-2-[18F]fluoro-trehalose ([18F]FDT), 2-deoxy-2-[18F]fluoro-laminaribiose ([18F]FDL), and 2-deoxy-2-[18F]fluoro-cellobiose ([18F]FDC). We subsequently tested [18F]FDM and [18F]FSK *in vitro*, showing accumulation by several clinically relevant pathogens including *Staphylococcus aureus* and *Acinetobacter baumannii*, and demonstrated their specific uptake *in vivo*. Both [18F]FDM and [18F]FSK were stable in human serum with high accumulation in preclinical infection models. The synthetic ease and high sensitivity of [18F]FDM and [18F]FSK to *S. aureus* including methicillin-resistant (MRSA) strains strongly justify clinical translation of these tracers to infected patients. Furthermore, this work suggests that chemoenzymatic radiosyntheses of complex [18F]FDG-derived oligomers will afford a wide array of PET radiotracers for infectious and oncologic applications.
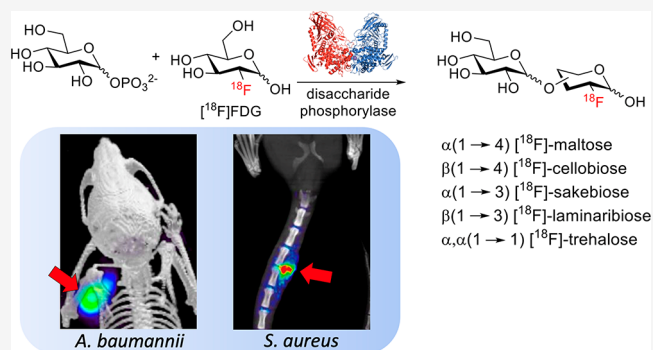
■ INTRODUCTION

Biocatalysis is now frequently used in chemical synthesis, both for the development of new building blocks and late-stage modification of complex molecules.[1] Chemoenzymatic syntheses of polysaccharides are particularly appealing, given the challenges of regioselectivity and stereoselectivity using standard organic methods.[2,3] Glucose-based polysaccharides are amenable to enzymatic incorporation of unnatural monosaccharide units, suggesting the possibility of using the common clinical imaging tracer 2-deoxy-[18F]-fluoro-D-glucose ([18F]FDG) as a synthon for building complex glycans compatible with *in vivo* positron emission tomography (PET) imaging. The use of enzymes to catalyze reactions involving the short half-life radionuclide fluorine-18 (half-life = 109.7 min) has been reported, notably using fluorinase.[4−6] Both chemical and enzymatic transformations of [18F]FDG represent promising ways to develop new imaging tools, given the wide availability of this tracer. For example, [18F]FDG can

(1) be reduced with $NaBH_4$ to produce the *Enterobacteriaceae*-targeted PET radiotracer 2-deoxy-[18F]-fluoro-D-sorbitol ([18F]FDS),[7,8] (2) be derivatized with amines and other substituents to yield analyte-sensitive "caged" prodrugs,[9,10] and (3) be employed as a prosthetic group to label drugs and peptide structures.[11,12] These approaches can be used to easily transform [18F]FDG into tracers targeting bacterial metabolism, the tumoral microenvironment, or specific oncologic targets, for example, the prostate-specific membrane antigen (PSMA) found in prostate cancer.

A

A

| EC	Name	Family	Precursor	Product
2.4.1.8	maltose phosphorylase	GH65	β-Glc-1P	Glc-α1,4-Glc
2.4.1.20	cellobiose phosphorylase	GH94	α-Glc-1P	Glc-β1,4-Glc
2.4.1.31	laminaribiose phosphorylase	GH94	α-Glc-1P	Glc-β1,3-Glc
2.4.1.64	trehalose phosphorylase	GH65	β-Glc-1P	Glc-α1,α1-Glc
2.4.1.279	sakebiose phosphorylase	GH65	β-Glc-1P	Glc-α1,3-Glc

B

Figure 1. (A) Partial list of disaccharide phosphorylases with the potential for the chemoenzymatic synthesis of disaccharides via reverse phosphorolysis. (B) Reverse phosphorolysis of substrates using disaccharide phosphorylase with either α- or β-glucose-1-phosphate.
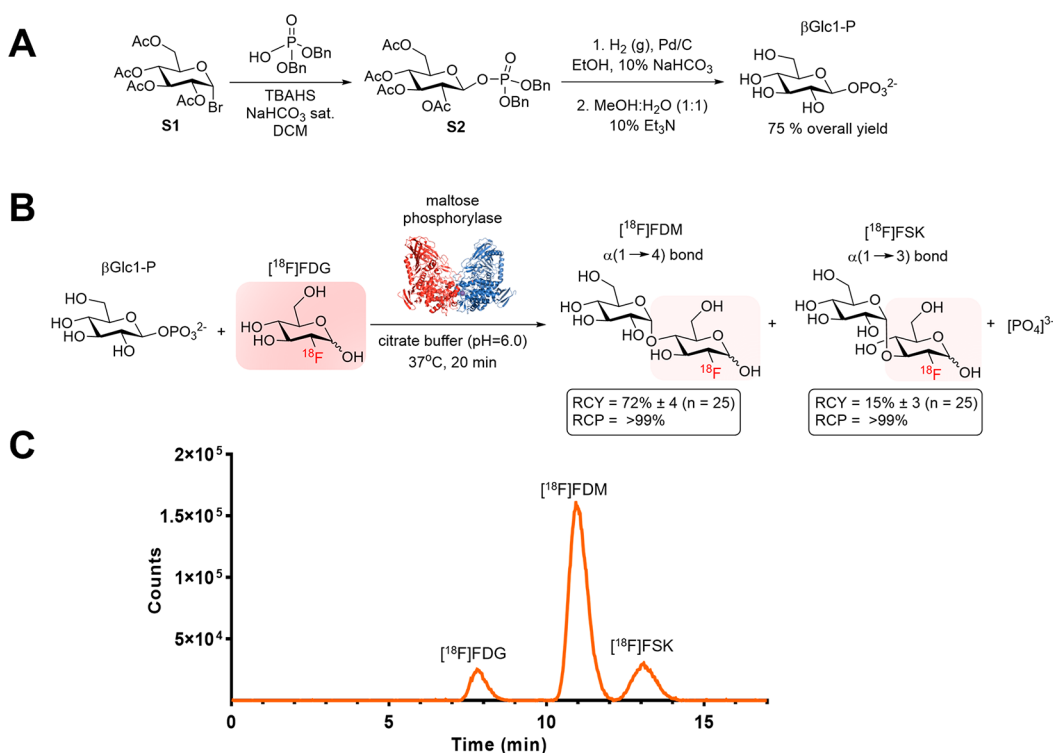
**Figure 2.** Radiochemical syntheses of 2-deoxy-2-[^{18}F]fluoro-maltose ([^{18}F]FDM) and 2-deoxy-2-[^{18}F]fluoro-sakebiose ([^{18}F]FSK). (A) Synthesis of the β-D-glucose-1-phosphate (βGlc1-P) precursor starting from acetobromo-α-D-glucose (**S1**). (B) Enzymatic radiosynthesis of [^{18}F]FDM and [^{18}F]FSK from 2-deoxy-2-[^{18}F]fluoro-D-glucose [^{18}F]FDG and βGlc1-P using maltose phosphorylase. (C) Radio HPLC analysis of crude products using a YMC-Pack Polyamine II column.

Our previous studies describing molecular tools for bacterial infection have focused on PET tracers labeling the bacterial cell wall, including D-[3-^{11}C]alanine[13] and D-[methyl-^{11}C]-methionine,[14−16] as well as the folic acid pathway using α-[^{11}C]PABA.[17] In addition to maltose-derived PET radiotracers, there have been several elegant methods in the past decade applied to bacteria using siderophore-derived probes,[18,19] radiolabeled trimethoprim derivatives,[20] and [^{18}F] sugar alcohols including [^{18}F]FDS[7] and 2-deoxy-[^{18}F]-fluoro-D-mannitol.[21] The most advanced radiotracer in bacteria-specific PET imaging is [^{18}F]FDS, which has been studied in numerous advanced preclinical models of infection as well as in infected patients.[22] A recent innovation in [^{18}F]FDS is its rapid, kit-based, and on-demand radiosynthesis from [^{18}F]FDG.[23] One limitation of [^{18}F]FDS is the lack of sensitivity for Gram-positive pathogens, which are major causes of musculoskeletal infections including vertebral discitis-osteomyelitis (VDO).[24,25] Therefore, we and others have a sustained interest in developing [^{18}F]-labeled PET tracers targeting *S. aureus* and other Gram-positive organisms.

In the study presented here, we used readily available [^{18}F]FDG to construct [^{18}F]-labeled dimers in one step via chemoenzymatic syntheses. This approach contrasts with most chemical methods reported to generate [^{18}F]glycans, which typically use a structurally complex/protected precursor and [^{18}F]fluoride incorporation via S$_N$2 displacement at sterically
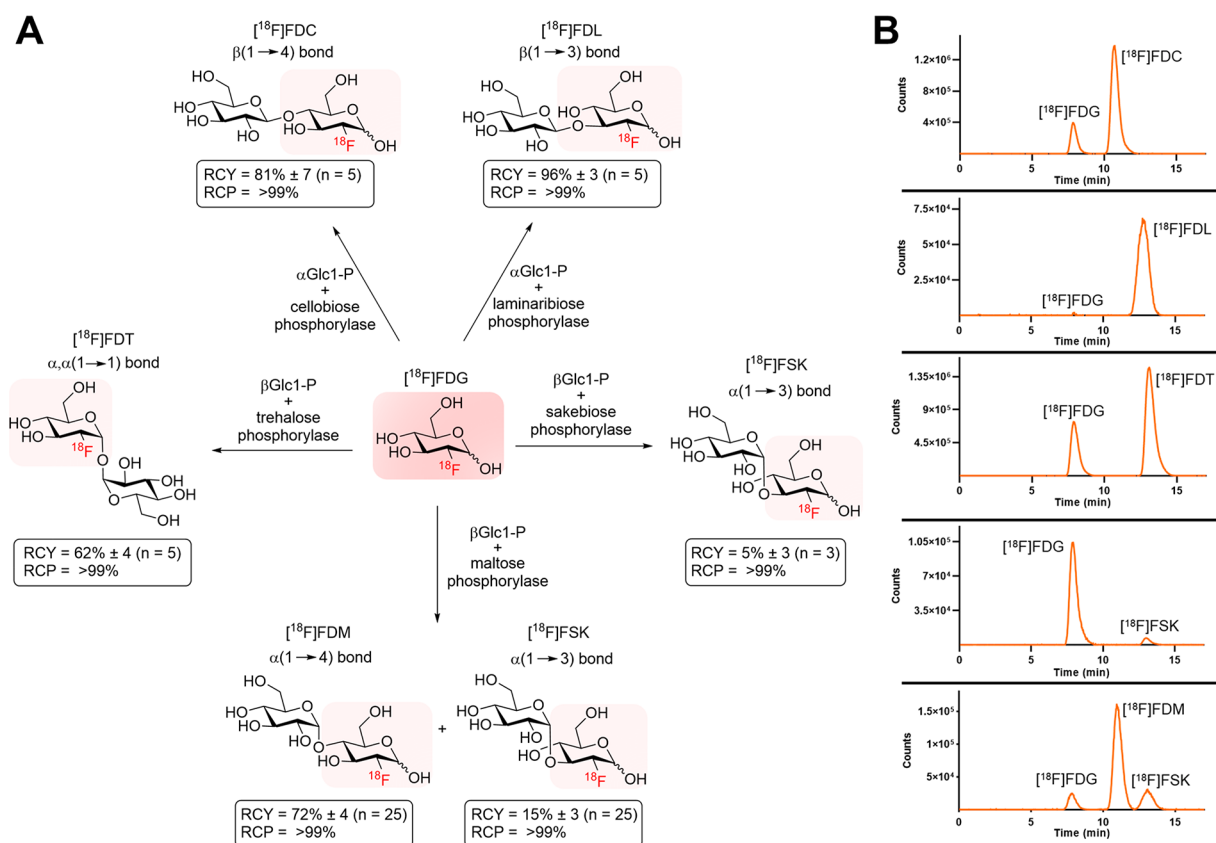
Figure 3. (A) Chemoenzymatic radiosyntheses of [18F]FDT, [18F]FDL, [18F]FDC, [18F]FDM, and [18F]FSK from [18F]FDG. All reactions were carried out at 37 °C, stirring for 20 min, using 6 mg (0.020 mmol) of precursor, 0.3 mg of enzyme (3−6 units), and 10−15 mCi [18F]FDG in 0.5 mL of citrate buffer (0.1 M, pH = 6.0). (B) Radio HPLC analysis of each enzymatic reaction using a YMC-Pack Polyamine II column.

amenable sites.[26] Based on prior work, a phosphorylase-catalyzed approach appeared feasible,[27−31] with several glucose-derived dimers highlighted in Figure 1A. Phosphorylases (glycosyltransferases, E.C. 2.4) are enzymes that catalyze the addition of an inorganic phosphate group to a carbohydrate acceptor by breaking an *O*-glycosidic bond. This reaction can be run "in reverse" to construct disaccharides from D-glucose-1-phosphate and a glucose derivative (Figure 1B). This strategy might therefore be used to rapidly fabricate [18F]-labeled disaccharides from [18F]FDG.

The first radiotracer we aimed to synthesize using this enzymatic method was the maltose-derived tracer 2-deoxy-[18F]-fluoro-maltose ([18F]FDM). Our interest in this probe was based on the potential specificity of microbial maltose metabolism[32−34] and the recent development of maltodextrin transporter-targeted imaging methods.[35−38] Maltodextrin (D-glucose units with α-1,4-glycosidic linkages) and its structural relatives are important energy sources for bacteria. These oligosaccharides are taken up by the maltodextrin transporter, which are present in both Gram-positive and Gram-negative bacterial species but are not found in mammalian cells. In order to enzymatically obtain [18F]FDM from [18F]FDG, we focused on commercially available maltose phosphorylase (E.C. 2.4.1.8), which has been used to synthesize a variety of disaccharides.[39−43]

In this work, we report the one-step radiosyntheses of [18F]FDM and α-1,3-product 2-deoxy-2-[18F]-fluoro-sakebiose ([18F]FSK) from easily accessible [18F]FDG using maltose phosphorylase as a catalyst. Both newly reported [18F]-labeled radiotracers were accumulated by important human pathogens,

including *S. aureus*, and were specific to bacterial infection *in vivo*. This phosphorylase-catalyzed method was extended to additional [18F]-labeled disaccharides of high biomedical interest, including 2-deoxy-2-[18F]fluoro-trehalose ([18F]FDT), 2-deoxy-2-[18F]fluoro-laminaribiose ([18F]FDL), and 2-deoxy-2-[18F]fluoro-cellobiose ([18F]FDC).

RESULTS

Maltose Phosphorylase-Catalyzed Radiosynthesis of [18F]FDM from Clinical [18F]FDG Showed the α-1,3 Product [18F]FSK as a Minor Product. Our initial goal was to demonstrate that the phosphorylase-catalyzed synthesis of an [18F] disaccharide from clinical [18F]FDG was a viable alternative to conventional radiochemical approaches. Although several bacteria-specific glycans could be constructed chemoenzymatically, we focused on maltose-derived PET radiotracers given the strong literature precedent.[36−38] We therefore synthesized the [18F]FDG-derived, 2-position-labeled [18F]FDM to target the bacterial maltose receptor. First, the precursor β-D-glucose-1-phosphate (βGlc1-P) was synthesized in three steps starting from acetobromo-α-D-glucose (**S1**) with a 75% overall yield (Figure 2A). Cyclotron-produced [18F]FDG was then directly added to a mixture of βGlc1-P and maltose phosphorylase in citrate buffer (0.1 M, pH 6.0) and stirred at 37 °C for 20 min. The reaction led to the formation of [18F]FDM with a 72 ± 4% decay-corrected radiochemical yield (RCY) and the α-1,3-linked product [18F]FSK with a 15 ± 3% decay-corrected RCY (N = 25) (Figure 2B). These yields were similar when high molar activity [18F]FDG was used, i.e., when "cold" glucose was
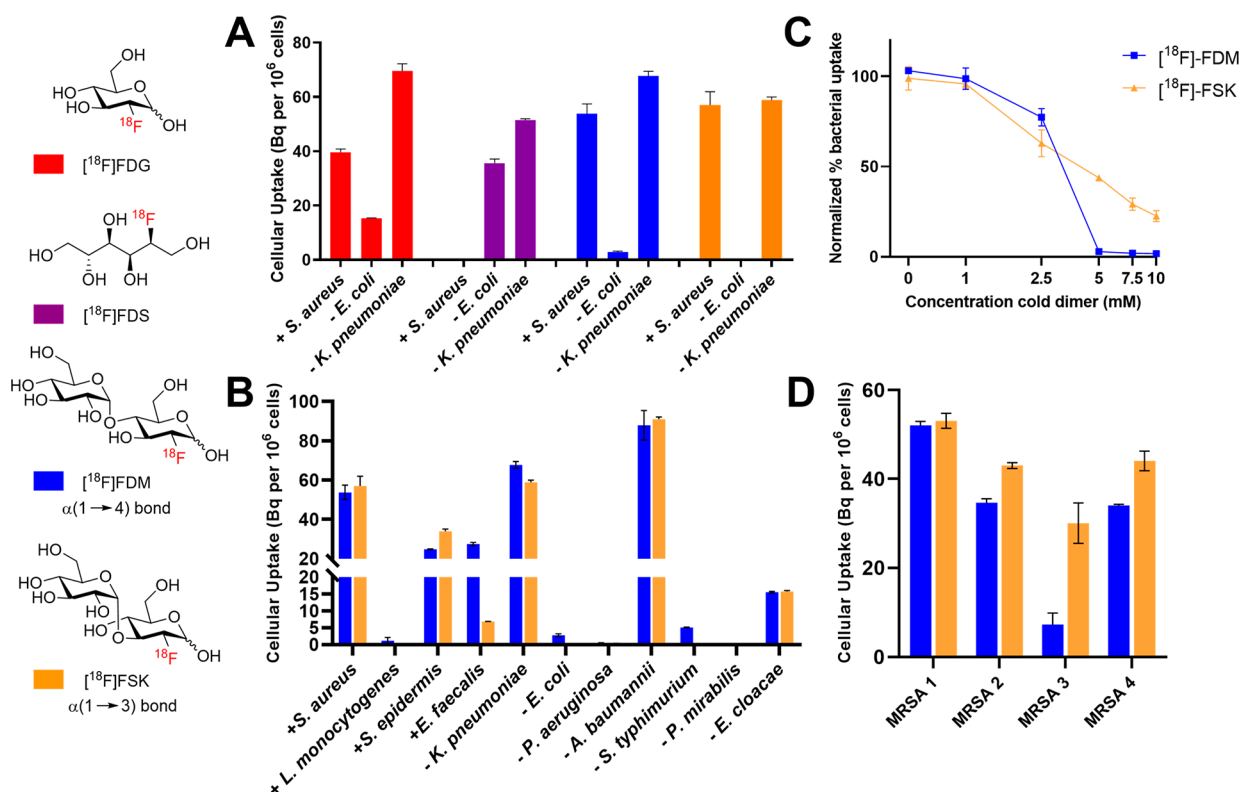
Figure 4. (A) *In vitro* bacteria uptake for [18F]FDG, 2-deoxy-2-[18F]-fluoro-D-sorbitol ([18F]FDS), [18F]FDM, and [18F]FSK. (B) *In vitro* bacteria uptake of [18F]FDM and [18F]FSK in Gram-positive and Gram-negative pathogens. (C) Accumulation of [18F]FDM and [18F]FSK in *S. aureus* with increasing concentrations of unlabeled maltose and sakebiose, respectively. (D) *In vitro* bacteria uptake of [18F]FDM and [18F]FSK in methicillin-resistant *S. aureus* (MRSA) clinical strains.

removed chromatographically from the clinical [18F]FDG sample (Supporting Information Figure S1) and when [18F]FDG was obtained from a commercial source (Supporting Information Figure S2). Each [18F]-labeled product was isolated using semipreparatory HPLC (Figure 2C) followed by formulation for subsequent *in vitro* and *in vivo* studies.

Phosphorylase-Catalyzed Radiosyntheses of [18F]FDT, [18F]FDL, and [18F]FDC from Clinical [18F]FDG. Several additional [18F]-labeled disaccharides might be used to image important human pathogens *in vivo*. The unique metabolism of the α,α-1,1-linked disaccharide trehalose by *Mycobacterium tuberculosis* has been previously targeted for therapy and imaging.[44−47] The β-linked disaccharides laminaribiose and cellobiose could potentially be leveraged for the metabolic imaging of fungal infections given the presence of β-1,3 and β-1,4 linkages in β-D-glucans (BDG), found in the cell walls of fungi.[48−50] An existing clinical assay (serum and cerebrospinal fluid) detects fungal β-1,3 linkages via the coagulation cascade of the horseshoe crab to detect invasive fungal infections caused by *Aspergillus* and *Candida* species.[51] With these potential imaging applications in mind, we attempted [18F]-radiosyntheses of the additional disaccharides indicated in Figure 1A. The use of trehalose-, cellobiose-, and laminaribiose-phosphorylase in combination with [18F]FDG and adequate α- or β-D-glucose-1-phosphate precursor led to the formation of [18F]FDT (decay-corrected RCY 62 ± 4%; N = 5), [18F]FDL (decay-corrected RCY 96 ± 3%; N = 5), and [18F]FDC (decay-corrected RCY 81 ± 7%; N = 5) (Figure 3). Of note, direct radiosynthesis of [18F]FSK via sakebiose phosphorylase produced only a modest yield of the desired product (decay-corrected RCY 5 ± 3%; N = 5). The [18F]FSK

tracer was therefore obtained via maltose phosphorylase as described above for subsequent *in vitro* and *in vivo* studies.

***In Vitro* Studies Using [18F]FDM and [18F]FSK Showed High Tracer Accumulation in Key Human Pathogens Including *S. aureus* and *A. baumannii*.** We hypothesized that the disaccharides [18F]FDM and [18F]FSK would have microbial sensitivity different from that of previously reported tracers, with accumulation in the key human pathogen *S. aureus*. We therefore studied these tracers *in vitro* to assess their incorporation into a variety of clinically relevant bacteria and establish microbial specificity. The Gram-positive organism *S. aureus* and the Gram-negative organisms *Escherichia coli* and *Klebsiella pneumoniae* were used to assess assimilation of [18F]FDM and [18F]FSK and compare their uptake to that of reported PET tracers [18F]FDG and [18F]FDS (Figure 4A). The glucose derivative [18F]FDG, used frequently in the clinic for oncologic and neuroimaging applications, was incorporated into all three bacteria. In contrast, as expected [18F]FDS accumulated in *E. coli* and *K. pneumoniae* but not *S. aureus*.[7] Both [18F]FDM and [18F]FSK showed a high incorporation in *S. aureus* and *K. pneumoniae*, similar to that of [18F]FDG, but low uptake in *E. coli*. A larger panel of bacterial pathogens was studied using [18F]FDM, [18F]FSK, and [18F]FDT. (Figure 4B, Supporting Information Figure S3). Overall, [18F]FDM and [18F]FSK demonstrated similar sensitivities toward Gram-positive and Gram-negative bacteria. They showed high uptake in *Staphylococcus epidermis*, *A. baumannii*, and *Enterobacter cloacae* but low uptake in *E. coli*, *Listeria monocytogenes*, *Pseudomonas aeruginosa*, *Salmonella typhimurium*, and *Proteus mirabilis*. Interestingly, [18F]FDT showed significant incorporation by *E. coli* (∼ 20 Bq/10^6 CFUs). There was only a
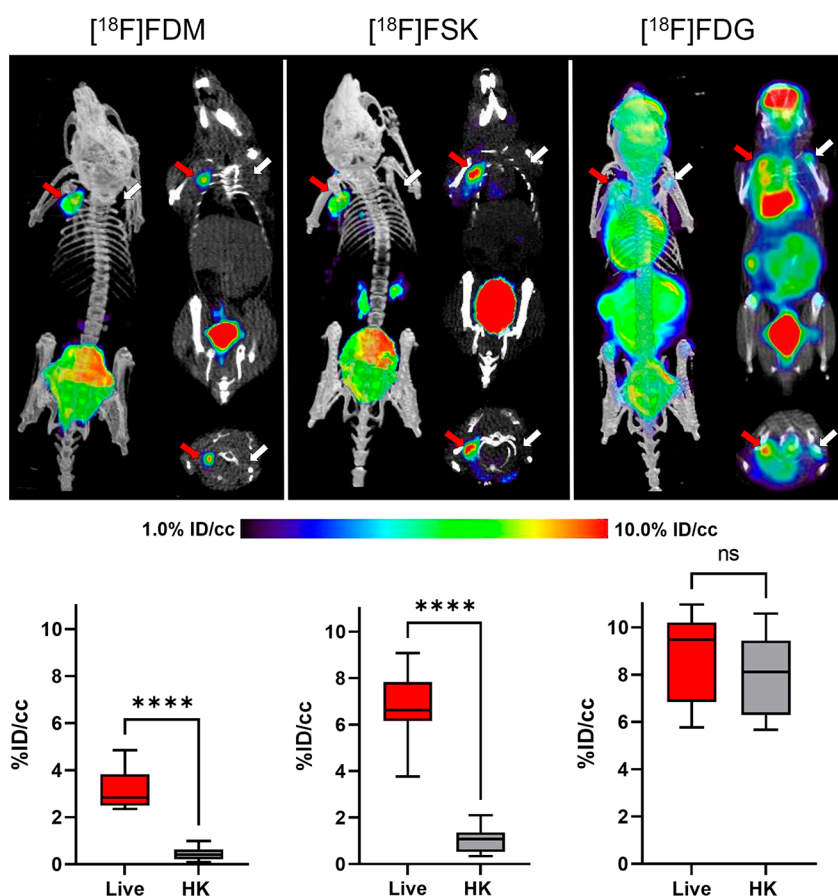
Figure 5. μPET-CT imaging of MRSA myositis in mice with $[^{18}F]FDM$, $[^{18}F]FSK$, and $[^{18}F]FDG$. The red arrows indicate the site of inoculation with live bacteria, while the white arrows correspond to heat-killed bacteria. The corresponding bar graphs indicate region-of-interest (ROI) analysis. As reflected by the images, the mean $[^{18}F]FDM$ and $[^{18}F]FSK$ accumulation for tissues infected with live bacteria was respectively 6.1- and 6.5-fold higher than that seen for heat-killed inoculation ($P < 0.0001$). In contrast, this difference was not seen for $[^{18}F]FDG$.

background level of incorporation of $[^{18}F]FDM$ and $[^{18}F]FSK$ into heat-killed bacteria for all species studied (Supporting Information Figure S4). $[^{18}F]FDM$ and $[^{18}F]FSK$ demonstrated increased bacterial accumulation over time in bacterial cultures (Supporting Information Figure S5) and showed a high degree of retention in "efflux" experiments (Supporting Information Figure S6). The uptake of $[^{18}F]FDM$ and $[^{18}F]FSK$ in *S. aureus* was inhibited in a dose-dependent manner by increasing concentrations of unlabeled maltose and unlabeled sakebiose (Figure 4C), and $[^{18}F]FSK$ uptake was inhibited in a dose-dependent manner by unlabeled maltose (Supporting Information Figure S7). As relatively high concentrations of unlabeled sugars were required to inhibit uptake and noting that unlabeled maltose inhibited $[^{18}F]FSK$ accumulation, we tested whether the known maltose transport system was involved. Uptake into *S. aureus* strains harboring transposon insertions within *malK* or *malE* genes (encoding the maltose ABC transporter ATP-binding proteins) or into the *malF* or *malG* genes (encoding maltose ABC transporter permeases) partially blocked $[^{18}F]FDM$ uptake but not $[^{18}F]FSK$ uptake (Supporting Information Figure S8). This latter finding suggests that $[^{18}F]FSK$ utilizes an alternative uptake mechanism. To investigate strain-to-strain variability in tracer accumulation, we studied additional clinical isolates of both methicillin-sensitive and methicillin-resistant *S. aureus* (MSSA; MRSA), *E. coli*, and *K. pneumoniae* (Figure 4D; Supporting Information Figure S9). For MRSA, three of the

isolates exhibited similar levels of uptake for both tracers, whereas one isolate showed a diminished uptake of $[^{18}F]FDM$.

$[^{18}F]FDM$ and $[^{18}F]FSK$ Are Stable in Human Serum and Their Degradation in Mouse Serum Can Be Abrogated by Use of an α-Glucosidase Inhibitor. In preparation for *in vivo* studies in mice and humans, we assessed the stability of $[^{18}F]FDM$ and $[^{18}F]FSK$ incubated with mouse and human serum using radio HPLC. In mouse serum, both radiotracers exhibited increasing time-dependent hydrolysis to $[^{18}F]FDG$, while they remained stable in human serum (Supporting Information Figure S10). This observation may be explained by the increased abundance of α-glucosidase, which has been reported to hydrolyze maltodextrin-based tracers,[52] in murine versus human serum. The α-glucosidase enzyme is predicted to degrade maltose from the nonreducing end, hydrolyzing $[^{18}F]FDM$ and $[^{18}F]FSK$ to glucose and $[^{18}F]FDG$ (Supporting Information Figure S11). In contrast, α-amylase (EC 3.2.1.1), which is present in human serum, degrades maltodextrin from the reducing end. Unlike longer-chain maltodextrin-based tracers (>3 units), $[^{18}F]FDM$ and $[^{18}F]FSK$ would be anticipated to be resistant to α-amylase and thus stable in human serum.[52]

We therefore tested the ability of the α-glucosidase inhibitors voglibose, acarbose, and miglitol (Supporting Information Figure S12), which are commonly used as a diabetes treatment, to prevent the α-glucosidase-mediated degradation of $[^{18}F]FDM$ and $[^{18}F]FSK$ in mouse serum. First,
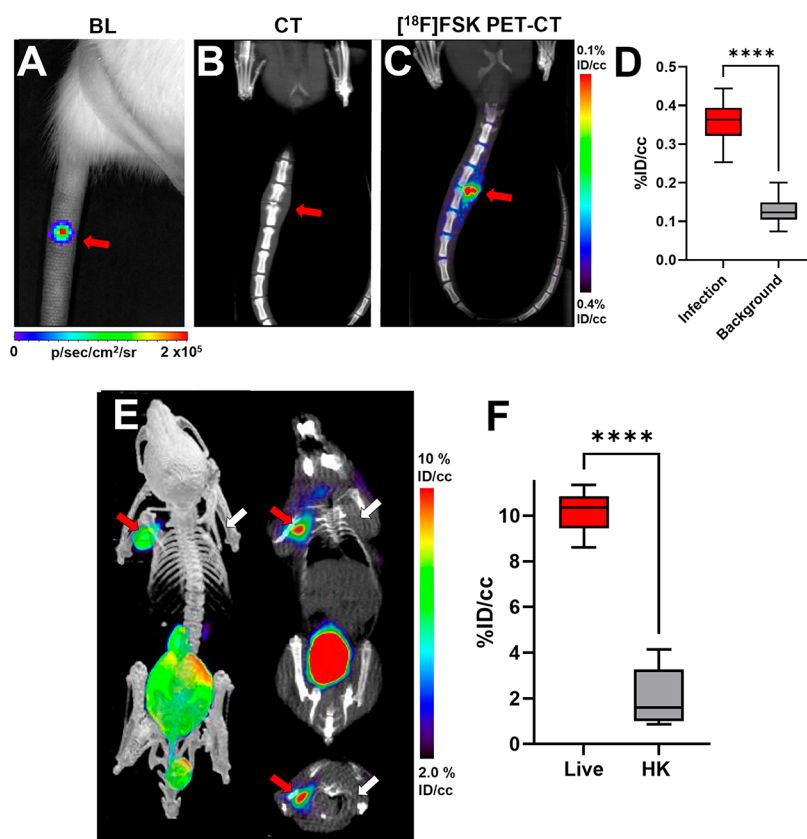
Figure 6. Imaging of *S. aureus* in vertebral discitis-osteomyelitis (VDO) rat models and *A. baumannii* in a myositis mouse model using [^{18}F]FSK. (A) Optical tomography image of a rat tail showing the bioluminescent signal from *S. aureus* Xen29 inoculation. (B) Computed tomography study performed at 10 days highlights the similarity between rodent and human discitis osteomyelitis. (C) PET/CT imaging of *S. aureus* Xen29 vertebral discitis-osteomyelitis (VDO) in rat ($N = 5$) with [^{18}F]FSK. (D) ROI analysis showing increased signal in segments inoculated with live bacteria versus background ($P < 0.0001$). (E) PET/CT imaging of *A. baumannii* myositis in mice ($N = 6$) with [^{18}F]FSK. The red arrows indicate the site of inoculation with live bacteria, while the white arrows correspond to heat-killed bacteria. (F) ROI analysis showing an increased signal in infected muscle versus inflammation ($P < 0.0001$).

we verified that voglibose and miglitol did not affect the accumulation of [^{18}F]FDM and [^{18}F]FSK in culture-grown *S. aureus*, whereas acarbose did (Supporting Information Figure S13). We then compared the inhibitor potency in mouse serum and found that voglibose was the most potent inhibitor for preventing [^{18}F]FDM and [^{18}F]FSK degradation (Supporting Information Figure S14). Together, these studies suggested that the concurrent administration of voglibose with [^{18}F]FDM and [^{18}F]FSK in murine studies allowed a better approximation for future human performance. An α-glucosidase inhibitor was not used in planned human studies. Finally, the stability of [^{18}F]FDM and [^{18}F]FSK was also assessed in human liver microsomes (HLM) (Supporting Information Figure S15), since many drugs are metabolized by the liver. Both tracers stayed stable in HLM for over 1 h, further supporting translational studies.

***In Vivo* Analysis of [^{18}F]FDM and [^{18}F]FSK in a Murine Model of Bacterial Infection Demonstrated Higher Signal to Background for the Sakebiose-Derived Tracer.** We first tested [^{18}F]FDM and [^{18}F]FSK in non-infected mice both to assess tracer stability and to detect potential contributions of the normal microbiome to tracer signals. When voglibose was added to tracer injection, *in vivo* analysis of [^{18}F]FDM and [^{18}F]FSK in conventionally raised mice[13] ($N = 5$), which have bacteria colonization of their gut, showed a background signal only in the kidney and bladder

(Supporting Information Figure S16). In contrast, when voglibose was omitted from the injection of [^{18}F]FDM and [^{18}F]FSK, the resulting signal was similar to that of [^{18}F]FDG, with high heart and brain uptake, demonstrating the utility of the inhibitor (Supporting Information Figure S17).

We next evaluated a murine model of acute bacterial infection to test whether [^{18}F]FDM and [^{18}F]FSK uptake could detect live bacteria in *in vivo* mouse models of infection. We chose the MRSA myositis model as it has been studied extensively in tracer development and used to compare tracer accumulation in infected tissues (harboring live bacteria) versus sterile inflammation (reflecting the host immune response).[7,13,14,17] Mice were inoculated with live MRSA in the left shoulder and with a 10-fold-higher dose of heat-killed MRSA in the right shoulder. Following tracer injection in the presence of voglibose, both [^{18}F]FDM and [^{18}F]FSK accumulated at the site of injection of live MRSA but not of heat-killed MRSA ($N = 6$ for each tracer; Figure 5). The region-of-interest (ROI) analysis revealed that [^{18}F]FDM and [^{18}F]FSK uptake at the side of live MRSA injection was 6.1- and 6.5-fold higher ($P < 0.0001$), respectively, than on the side of the heat-killed MRSA injection. These results were further corroborated by *ex vivo* analysis (tissue harvesting and gamma counting) which showed that the mean [^{18}F]FDM and [^{18}F]FSK accumulation in tissues inoculated with live MRSA was respectively 3.8- and 4.7-fold higher than that seen for

tissues inoculated with heat-killed bacteria ($P = 0.001$ for [18F]FDM and $P < 0.0001$ for [18F]FSK) (Supporting Information Figures S18 and S19). In contrast, the glucose-transporter-targeted parent tracer [18F]FDG accumulated equally at injection sites inoculated with either live or heat-killed MRSA, as quantified by *in vivo* and *ex* vivo analysis (Supporting Information Figure S20). We thus conclude that both the [18F]FDM and [18F]FSK tracers are specific for live versus heat-killed MRSA and have the potential to distinguish bacterial inflammation from sterile inflammation. However, as [18F]FSK proved to have better *in vivo* performance than [18F]FDM, it was chosen for testing in additional preclinical models.

Preclinical Models of Vertebral Discitis-Osteomyelitis and *A. baumannii* Myositis Suggested That [18F]FSK Could Be Used in Challenging Clinical Settings. Based on our encouraging results with MRSA *in vitro* and in the murine myositis model, we next studied a rat model of vertebral discitis-osteomyelitis using [18F]FSK. Rats were inoculated with live *S. aureus* (Xen-29, bioluminescent strain) in the third intervertebral space from the base of the tail and with heat-killed *S. aureus* (Xen-29) in the fifth intervertebral space. The tail was imaged by luminescence emission using a Xenogen IVIS 50 to verify the location and presence of the bacterial infection (Figure 6a). After 4 days, CT was used to image damage to the disc and bone, revealing the development of disc-space narrowing and end-plate degeneration, which mimic human bacterial spinal infections (Figure 6b). Imaging of the tail using [18F]FSK was performed at day 4 ($N = 5$) and day 10 ($N = 3$) following the inoculation of bacteria (Figure 6c and Supporting Information Figures S21 and S22). In both cases, [18F]FSK accumulated at the infection site, with ROI analyses demonstrating 2.8-fold higher signals at day 4 ($P < 0.0001$) and 3.1-fold higher signals at day 10 ($P < 0.0001$), in the third intervertebral space versus the fifth intervertebral space (Figure 6d and Supporting Information Figure S22).

After showing the efficacy of [18F]FSK *in vivo* to detect *S. aureus* infection, we further studied *A. baumannii* in the murine myositis model, as it is a common cause of soft tissue infections in the battlefield. We injected *A. baumannii* as described above and performed μPET/CT following [18F]FSK injection. The tracer accumulated at the site of live *A. baumannii* injection into the left shoulder but not at the site of heat-killed *A. baumannii* injection into the right shoulder (Figure 6e). ROI analysis revealed that [18F]FSK accumulation in the live *A. baumannii* injected muscle was 4.9-fold higher than at the heat-killed *A. baumannii* injected muscle ($P < 0.0001$) (Figure 6f). *Ex vivo* analysis revealed that tracer uptake at the site of live *A. baumannii* injection was 3.9-fold higher compared to the site of heat-killed *A. baumannii* injection ($P < 0.0001$) (Supporting Information Figure S23). Together, these studies employing two clinically important human bacterial pathogens, *S. aureus* and *A. baumannii*, in two different murine models that mimic the challeng of treating human infections demonstrate the potential of using [18F]FSK to image human bacterial infections in the clinic.

■ DISCUSSION

Bacteria-specific metabolic pathways have been exploited by antimicrobial agents for decades, with infection imaging being a more recent application of this approach. In recent years, numerous compelling methodologies have been further validated in patients most notably [18F]FDS, which is highly sensitive for *Enterobacteriaceae* and which can be efficiently radiosynthesized from the common tracer [18F]FDG,[23] making it a more practical tool for potential clinical use. To further impact infectious disease management in the clinic, we will require imaging tools with both straightforward radiosyntheses and applicability to a broader range of bacteria, including the common human Gram-positive bacteria *S. aureus*.

Tracers labeled with radionuclides with a shorter half-life [11C; $t_{1/2} = 20$ min][13,15,17] or studied primarily in academic centers [89Zr; $t_{1/2} = 78$ h][53] face significant challenges in the acute care/emergency setting, highlighting the need for infection imaging methods that might be more broadly useful. We therefore developed a chemoenzymatic method for pathogen-targeted PET radiotracers, benefiting from (1) the efficiency of chemoenzymatic reactions versus standard PET radiochemical methods and (2) the general availability of [18F]FDG as a synthon. A major challenge in the chemical synthesis of [18F]-labeled carbohydrates is the short half-life (109.7 min) of fluorine-18, requiring complex precursors, late-stage S_N2 radiofluorination via [18F]-fluoride, and less sterically hindered labeling sites.[26] In contrast, the current report describes a rapid (20 min), one-step radiosynthesis using [18F]FDG and commercially available precursors with high regioselectivity/stereoselectivity and potential metabolic advantages conferred via the 2-position [18F] labeling. With the goal of developing an on-demand *S. aureus*-sensitive tracer, we used maltose phosphorylase to dimerize [18F]FDG into the α-1,4 and α-1,3 disaccharides [18F]FDM and [18F]FSK. Both [18F]FDM and [18F]FSK showed outstanding performance characteristics in their ability to detect living bacteria *in vivo*, including *S. aureus*.

Sakebiose (also known as nigerose) has been described as an "uncommon sugar" and investigated for its potential as an alternative sweetener, oral probiotic, and immunopotentiating therapy.[54−56] Most published work on sakebiose has focused on the production of the disaccharide via the enzymatic degradation of dextrans or synthesis using phosphorylases, whose activity may be modified via mutagenesis.[57−60] Microbial transport and metabolism of sakebiose are incompletely understood, and the metabolism of sakebiose and [18F]FSK may not be identical. *S. aureus* maltodextrin transporter mutants accumulated [18F]FSK similar to the wild type, suggesting that [18F]FSK and potentially sakebiose itself have alternative or additional transport mechanisms. Additional studies are needed to better understand these mechanisms and potentially drive the discovery of new metabolic imaging tools.

As stated previously, we believe that [18F]FDM and [18F]FSK have outstanding potential as clinical PET tracers, especially for the detection and monitoring of *S. aureus* infections. Both can be produced quickly and efficiently from widely available [18F]FDG, without the need for regioselective precursor modification and chemical protection/deprotection. Most interestingly, the 2-position [18F]-substituted maltose derivative appears to confer numerous advantages over the 6-position [18F] derivative originally reported by Namavari et al.[37,61] in terms of stability and microorganism export. Although the 6-position is more chemically accessible, the corresponding 6-[18F] derivative is both more vulnerable to defluorination and prohibits 6-position phosphorylation, which is a major mechanism of [18F]FDG retention (via hexokinase, E.C. 2.7.1.1). Indeed, in terms of *in vitro* stability, bacterial export, and *in vivo* performance [18F]FDM and [18F]FSK more closely mimic the "second generation" PET tracer 6″-[18F]-

fluoromaltotriose.[38,62] An explicit comparison between [^{18}F]-labeled α-1,4 linked oligomers (maltose, maltotriose, and maltohexaose) would be helpful to guide clinical implementation and is the basis of ongoing laboratory efforts. An additional challenge to clinical implementation suggested by our data is the variability in species and strain uptake for [^{18}F]FDM, [^{18}F]FSK, and [^{18}F]FDT, increasingly observed as bacteria-targeted tracers are more thoroughly studied. There are resulting "gaps" in microbe identification that could be addressed by the coadministration of multiple PET tracers. For example, the sorbitol derivative [^{18}F]FDS (also rapidly synthesized from [^{18}F]FDG) could be combined with [^{18}F]FSK for better coverage of *Enterobacteriaceae*. Furthermore, once a causative pathogen is identified in clinical practice, a tracer with a high established sensitivity could be used to follow an infection to resolution.

CONCLUSIONS

We have developed a chemoenzymatic method for the radiosyntheses of [^{18}F]-labeled disaccharides from the readily available precursor [^{18}F]FDG. The strategy was used to generate both α- and β-linked [^{18}F] disaccharides of high biomedical interest for pathogen-specific imaging, specifically [^{18}F]-labeled derivatives of maltose, sakebiose, trehalose, laminaribiose, and cellobiose. We anticipate that this approach may be used to construct other complex [^{18}F] glycans and facilitate the on-demand radiosynthesis of PET radiotracers for infection and other diseases.

MATERIALS AND METHODS

General Chemistry and Radiochemistry. Full descriptions of chemical and radiochemical syntheses as well as the analytical techniques used are provided in the Supporting Information. Unless otherwise noted, all of the reagents were obtained commercially and used without further purification. Radioisotopes were generated at the UCSF radiopharmaceutical facility.

Synthesis of β-D-Glucose-1-phosphate (βGlc1-P). β-D-Glucose-1-phosphate (βGlc1-P) was synthesized in three steps from 1-bromo-α-D-glucose tetraacetate (75% overall yield, gram scale). For detailed methods and the characterization of each compound, see the Supporting Information.

General Enzymatic Radiosynthesis of [^{18}F]FDC, [^{18}F]FDL, [^{18}F]FDT, [^{18}F]FDM, and [^{18}F]FSK. In a 4 mL borosilicate vial containing a PTFE stir bar, phosphorylase (0.3−0.5 mg, 3−6 units) and α- or β-Glc1-P (6 mg, 20 mmol) were added. A solution of [^{18}F]FDG (15−30 mCi) in citrate buffer (pH 6.0) was directly transferred to the vial, and the mixture was stirred at 37 °C for 20 min. The mixture was diluted with MeCN and then filtered through a C18 light cartridge and subsequently purified via semipreparative HPLC using YMC column Polyamine Pack II, 10 mm (73% MeCN/27% H$_2$O). The [^{18}F]-labeled disaccharide product was isolated in 5−7 mL fractions. The fractions were then diluted with MeCN (40 mL) before being passed through a Sep-pak Plus NH$_2$ cartridge at 5 mL/min to trap each dimer product. After the cartridge was flushed with air and N$_2$ gas, the tracer was eluted using a saline solution for direct formulation for *in vitro* or *in vivo* use. Radiochemical yields and the purity of the [^{18}F] product were confirmed by analytical HPLC. The total synthesis time (including purification and formulation) was 70 min. The synthesis and characterization of cold standards are described in the Supporting Information.

Uptake of [^{18}F]FDM and [^{18}F]FSK in Gram-Positive and Gram-Negative Bacteria *In Vitro*. *S. aureus, L. monocytogenes, S. epidermidis, E. faecalis, K. pneumoniae, E. coli, P. aeruginosa, A. baumannii, S. typhimurium, P. mirabilis*, and *E. cloacae* were grown overnight in lysogeny broth (LB) in a shaking incubator at 37 °C. Overnight cultures were diluted to an optical density at 600 nm (OD$_{600}$) of 0.05 and grown to the exponential phase (~0.4−0.6). Bacterial cultures were incubated with 24 μCi of [^{18}F]FDM and [^{18}F]FSK at 37 °C for 90 min for uptake studies and also at 30 and 60 min for temporal evaluation. After tracer incubation, 500 μL of the bacterial cultures were transferred to Spin-X LC 1.5 mL tubes (0.22 μm) and were centrifuged (6 min, 13 200 rpm) to separate the bacterial cells and supernatant. Bacterial cells were then washed once with phosphate-buffered saline (PBS) to remove any tracer not taken up by bacteria. Heat-killed bacterial samples used as controls were prepared by incubating the bacterial cultures at 90 °C for 30 min. Retained radiotracer within samples was then counted using an automated gamma counter (Hidex). Blocking experiments were performed by adding cold maltose (0.01−10 mM) together with 24 μCi of [^{18}F]FDM and [^{18}F]FSK and following the same protocol. Efflux experiments were performed by incubating the bacteria with 24 μCi of [^{18}F]FDM and [^{18}F]FSK for 30 min and then pelleting the bacteria and replacing the media with fresh LB. The cultures were then incubated for an additional 30 min, and then a similar method was used to separate the bacterial cells and supernatant. Radioactivity for both was counted using a gamma counter (HIDEX) to obtain residual activity.

Animal Experiments. All animal procedures were approved by the UCSF Institutional Animal Care and Use Committee and performed in accordance with UCSF guidelines. CBA/J mice (female, 8−10 weeks old) and Sprague/Dawley rats (female, 10−12 weeks old) were used for the experiments. Mice and rats were housed in individually ventilated cages under normal diet in groups of 3 rats or 5 mice, with ad libitum access to food and water throughout the experiment. Prior to infection and during imaging, the animals were anesthetized with 5% isoflurane. Mice and rats were inoculated with *S. aureus* Xen29, MRSA, *K. pneumoniae*, or heat-killed bacteria as described previously.[13] At different time points further specified below, the mice and rats were imaged using a Xenogen IVIS 50 instrument or Inveon μPET-CT following the injection of [^{18}F]FDM, [^{18}F]FSK, or [^{18}F]FDG.

***In Vivo* [^{18}F]FDM and [^{18}F]FSK Dynamic Imaging in a Myositis Mouse Model.** Mice were inoculated with MRSA or *A. baumannii* (~2 × 10^7 CFU) in the left deltoid muscle and a 10-fold-higher bacterial load of heat-killed bacteria in the right deltoid muscle. The bacterial cultures were prepared as previously reported.[13] After 12 h, [^{18}F]FDM or [^{18}F]FSK was injected via the tail vain (~100 μL, 200 μCi, containing 1 mg of voglibose). The mice were then imaged by μPET-CT using the same protocol previously described[13] (90 min dynamic PET scan, 5 min CT). The resulting μPET-CT images were analyzed with Amide's Medical Image Data Examiner, as described below.

***In Vivo* [^{18}F]FSK Dynamic Imaging in a VDO Rat Model.** *S. aureus* Xen29 was used to induce discitis in 5 Sprague/Dawley Rats (Charles River). Xen29 is a bioluminescent *S. aureus* strain that carries a stable copy of the *Photorhabdus luminescens* lux operon (*luxABCDE*) and was used in the study to verify successful bacterial inoculation in the third intervertebral space. Xen29 was grown overnight in LB containing 100 μg/L of kanamycin as previously described and diluted in PBS to obtain the desired bacterial load for infection (~2 × 10^7 colony forming units, CFU). Rats (*N* = 5) were inoculated with Xen29 live and heat-killed (10-fold higher bacterial load) in the third and fifth intervertebral spaces, respectively. At days 0 and 2, the rats were imaged using a Xenogen IVIS 50 imaging system to detect the bioluminescence signal and confirm the infection. At days 4 and 10, [^{18}F]FSK injection (~200 μL, 500 μCi, 5 mg of voglibose) was performed using a tail vein catheter. One hour after tracer injection, rats were transferred to the μPET-CT system (Siemens) and imaged using a 90 min dynamic PET acquisition scan followed by a 5 min μCT scan for attenuation correction and anatomical coregistration. Anesthesia was maintained during bioluminescence and μPET-CT imaging using 5% isofluorane. Resulting μPET-CT images were analyzed using AMIDE, and %ID/cc was used for quantitative comparison. %ID/cc values were established via the 8 mm^3 region of interest using the spherical tool. Region of interest analysis from resulting μPET-CT images 90 min after injection was used to

compare tracer performance. Resulting bioluminescence images were analyzed with Living Image Software 3.2.

DATA ANALYSIS AND STATISTICAL CONSIDERATIONS

For synthesis, the radiochemical yield incorporates a decay correction for ^{18}F ($t_{1/2}$ = 109.7 min). *In vitro* data were normalized to CFUs for sensitivity analysis to account for differential growth rates between organisms. All *in vivo* PET data were viewed by using open-source AMIDE software. Uptake quantification was performed by drawing spherical regions of interest (5−8 mm^3) over indicated organs on the CT portion of the exam and expressed as the percent injected dose per gram. All statistical analysis was performed using GraphPad Prism v 9. Data were analyzed using an unpaired two-tailed Student's *t* test. All graphs are depicted with error bars corresponding to the standard error of the mean.

ASSOCIATED CONTENT

⬛ Supporting Information

The Supporting Information is available free of charge at https://pubs.acs.org/doi/10.1021/jacs.3c03338.

Detailed information regarding synthesis and *in vitro* and *in vivo* experiments not reported in the main text (PDF)

AUTHOR INFORMATION

Corresponding Author

David M. Wilson − *Department of Radiology and Biomedical Imaging, University of California, San Francisco, San Francisco, California 94158, United States;* ⬤ orcid.org/0000-0002-1095-046X; Email: david.m.wilson@ucsf.edu

Authors

Alexandre M. Sorlin − *Department of Radiology and Biomedical Imaging, University of California, San Francisco, San Francisco, California 94158, United States*

Marina López-Álvarez − *Department of Radiology and Biomedical Imaging, University of California, San Francisco, San Francisco, California 94158, United States;* ⬤ orcid.org/0000-0001-5794-5951

Sarah J. Rabbitt − *Department of Radiology and Biomedical Imaging, University of California, San Francisco, San Francisco, California 94158, United States*

Aryn A. Alanizi − *Department of Radiology and Biomedical Imaging, University of California, San Francisco, San Francisco, California 94158, United States*

Rebecca Shuere − *Department of Radiology and Biomedical Imaging, University of California, San Francisco, San Francisco, California 94158, United States*

Kondapa Naidu Bobba − *Department of Radiology and Biomedical Imaging, University of California, San Francisco, San Francisco, California 94158, United States;* ⬤ orcid.org/0000-0001-6304-2855

Joseph Blecha − *Department of Radiology and Biomedical Imaging, University of California, San Francisco, San Francisco, California 94158, United States*

Sasank Sakhamuri − *Department of Radiology and Biomedical Imaging, University of California, San Francisco, San Francisco, California 94158, United States*

Michael J. Evans − *Department of Radiology and Biomedical Imaging, University of California, San Francisco, San Francisco, California 94158, United States;* ⬤ orcid.org/0000-0003-4947-1316

Kenneth W. Bayles − *Department of Pathology and Microbiology, University of Nebraska Medical Center, Omaha, Nebraska 68198, United States;* ⬤ orcid.org/0000-0001-9521-3540

Robert R. Flavell − *Department of Radiology and Biomedical Imaging, University of California, San Francisco, San Francisco, California 94158, United States;* ⬤ orcid.org/0000-0002-8694-1199

Oren S. Rosenberg − *Department of Medicine, University of California, San Francisco, San Francisco, California 94158, United States*

Renuka Sriram − *Department of Biotechnology, Ghent University, Gent B-9000, Belgium;* ⬤ orcid.org/0000-0003-3505-2479

Tom Desmet − *Department of Biotechnology, Ghent University, Gent B-9000, Belgium;* ⬤ orcid.org/0000-0002-5788-3022

Bernd Nidetzky − *Institute of Biotechnology and Biochemical Engineering,, Graz University of Technology, Graz 8010, Austria;* ⬤ orcid.org/0000-0002-5030-2643

Joanne Engel − *Department of Biotechnology, Ghent University, Gent B-9000, Belgium*

Michael A. Ohliger − *Department of Radiology and Biomedical Imaging, University of California, San Francisco, San Francisco, California 94158, United States; Department of Radiology, Zuckerberg San Francisco General Hospital, San Francisco, California 94110, United States*

James S. Fraser − *Department of Bioengineering and Therapeutic Sciences, University of California, San Francisco, San Francisco, California 94158, United States*

Complete contact information is available at: https://pubs.acs.org/10.1021/jacs.3c03338

ACKNOWLEDGMENTS

REFERENCES

(1) Winkler, C. K.; Schrittwieser, J. H.; Kroutil, W. Power of Biocatalysis for Organic Synthesis. *ACS Cent. Sci.* **2021**, 7 (1), 55−71.

(2) Kadokawa, J. Precision Polysaccharide Synthesis Catalyzed by Enzymes. *Chem. Rev.* **2011**, 111 (7), 4308−4345.

(3) Li, J.; Amatuni, A.; Renata, H. Recent Advances in the Chemoenzymatic Synthesis of Bioactive Natural Products. *Curr. Opin. Chem. Biol.* **2020**, 55, 111−118.

(4) Deng, H.; Cobb, S. L.; Gee, A. D.; Lockhart, A.; Martarello, L.; McGlinchey, R. P.; O'Hagan, D.; Onega, M. Fluorinase Mediated C−18F Bond Formation, an Enzymatic Tool for PET Labelling. *Chem. Commun.* **2006**, No. 6, 652.

(5) Winkler, M.; Domarkas, J.; Schweiger, L. F.; O'Hagan, D. Fluorinase-Coupled Base Swaps: Synthesis of [18F]-5′-Deoxy-5′-Fluorouridines. *Angew. Chem. Int. Ed* **2008**, *47* (52), 10141−10143.

(6) Zhang, Q.; Dall'Angelo, S.; Fleming, I. N.; Schweiger, L. F.; Zanda, M.; O'Hagan, D. Last-Step Enzymatic [(18) F]-Fluorination of Cysteine-Tethered RGD Peptides Using Modified Barbas Linkers. *Chem.—Eur. J.* **2016**, *22* (31), 10998−11004.

(7) Weinstein, E. A.; Ordonez, A. A.; DeMarco, V. P.; Murawski, A. M.; Pokkali, S.; MacDonald, E. M.; Klunk, M.; Mease, R. C.; Pomper, M. G.; Jain, S. K. Imaging Enterobacteriaceae Infection in Vivo with 18F-Fluorodeoxysorbitol Positron Emission Tomography. *Sci. Transl. Med.* **2014**, *6* (259), 259ra146.

(8) Li, Z.-B.; Wu, Z.; Cao, Q.; Dick, D. W.; Tseng, J. R.; Gambhir, S. S.; Chen, X. The Synthesis of 18F-FDS and Its Potential Application in Molecular Imaging. *Mol. Imaging Biol.* **2008**, *10* (2), 92−98.

(9) Flavell, R. R.; Truillet, C.; Regan, M. K.; Ganguly, T.; Blecha, J. E.; Kurhanewicz, J.; VanBrocklin, H. F.; Keshari, K. R.; Chang, C. J.; Evans, M. J.; Wilson, D. M. Caged [(18)F]FDG Glycosylamines for Imaging Acidic Tumor Microenvironments Using Positron Emission Tomography. *Bioconjugate Chem.* **2016**, *27* (1), 170−178.

(10) Liu, W.; Truillet, C.; Flavell, R. R.; Brewer, T. F.; Evans, M. J.; Wilson, D. M.; Chang, C. J. A Reactivity-Based [18F]FDG Probe for in Vivo Formaldehyde Imaging Using Positron Emission Tomography. *Chem. Sci.* **2016**, *7* (8), 5503−5507.

(11) Bouvet, V.; Wuest, M.; Bailey, J. J.; Bergman, C.; Janzen, N.; Valliant, J. F.; Wuest, F. Targeting Prostate-Specific Membrane Antigen (PSMA) with F-18-Labeled Compounds: The Influence of Prosthetic Groups on Tumor Uptake and Clearance Profile. *Mol. Imaging Biol.* **2017**, *19* (6), 923−932.

(12) Namavari, M.; Cheng, Z.; Zhang, R.; De, A.; Levi, J.; Hoerner, J. K.; Yaghoubi, S. S.; Syud, F. A.; Gambhir, S. S. A Novel Method for Direct Site-Specific Radiolabeling of Peptides Using [18F]FDG. *Bioconjugate Chem.* **2009**, *20* (3), 432−436.

(13) Parker, M. F. L.; Luu, J. M.; Schulte, B.; Huynh, T. L.; Stewart, M. N.; Sriram, R.; Yu, M. A.; Jivan, S.; Turnbaugh, P. J.; Flavell, R. R.; Rosenberg, O. S.; Ohliger, M. A.; Wilson, D. M. Sensing Living Bacteria in Vivo Using D-Alanine-Derived 11C Radiotracers. *ACS Cent. Sci.* **2020**, *6* (2), 155−165.

(14) Neumann, K. D.; Villanueva-Meyer, J. E.; Mutch, C. A.; Flavell, R. R.; Blecha, J. E.; Kwak, T.; Sriram, R.; VanBrocklin, H. F.; Rosenberg, O. S.; Ohliger, M. A.; Wilson, D. M. Imaging Active Infection in Vivo Using D-Amino Acid Derived PET Radiotracers. *Sci. Rep.* **2017**, *7* (1), 7903.

(15) Stewart, M. N.; Parker, M. F. L.; Jivan, S.; Luu, J. M.; Huynh, T. L.; Schulte, B.; Seo, Y.; Blecha, J. E.; Villanueva-Meyer, J. E.; Flavell, R. R.; VanBrocklin, H. F.; Ohliger, M. A.; Rosenberg, O.; Wilson, D. M. High Enantiomeric Excess In-Loop Synthesis of d-[Methyl-11C]Methionine for Use as a Diagnostic Positron Emission Tomography Radiotracer in Bacterial Infection. *ACS Infect. Dis.* **2020**, *6* (1), 43−49.

(16) Polvoy, I.; Seo, Y.; Parker, M.; Stewart, M.; Siddiqua, K.; Manacsa, H. S.; Ravanfar, V.; Blecha, J.; Hope, T. A.; Vanbrocklin, H.; Flavell, R. R.; Barry, J.; Hansen, E.; Villanueva-Meyer, J. E.; Engel, J.; Rosenberg, O. S.; Wilson, D. M.; Ohliger, M. A. Imaging Joint Infections Using D-Methyl-11C-Methionine PET/MRI: Initial Experience in Humans. *Eur. J. Nucl. Med. Mol. Imaging* **2022**, *49* (11), 3761−3771.

(17) Mutch, C. A.; Ordonez, A. A.; Qin, H.; Parker, M.; Bambarger, L. E.; Villanueva-Meyer, J. E.; Blecha, J.; Carroll, V.; Taglang, C.; Flavell, R.; Sriram, R.; VanBrocklin, H.; Rosenberg, O.; Ohliger, M. A.; Jain, S. K.; Neumann, K. D.; Wilson, D. M. [11C]Para-Aminobenzoic Acid: A Positron Emission Tomography Tracer Targeting Bacteria-Specific Metabolism. *ACS Infect. Dis.* **2018**, *4* (7), 1067−1072.

(18) Peukert, C.; Langer, L. N. B.; Wegener, S. M.; Tutov, A.; Bankstahl, J. P.; Karge, B.; Bengel, F. M.; Ross, T. L.; Brönstrup, M. Optimization of Artificial Siderophores as 68Ga-Complexed PET Tracers for In Vivo Imaging of Bacterial Infections. *J. Med. Chem.* **2021**, *64* (16), 12359−12378.

(19) Petrik, M.; Umlaufova, E.; Raclavsky, V.; Palyzova, A.; Havlicek, V.; Pfister, J.; Mair, C.; Novy, Z.; Popper, M.; Hajduch, M.; Decristoforo, C. 68Ga-Labelled Desferrioxamine-B for Bacterial Infection Imaging. *Eur. J. Nucl. Med. Mol. Imaging* **2021**, *48* (2), 372−382.

(20) Sellmyer, M. A.; Lee, I.; Hou, C.; Weng, C.-C.; Li, S.; Lieberman, B. P.; Zeng, C.; Mankoff, D. A.; Mach, R. H. Bacterial Infection Imaging with [18F]Fluoropropyl-Trimethoprim. *Proc. Natl. Acad. Sci. U. S. A.* **2017**, *114* (31), 8372−8377.

(21) Simpson, S. R.; Kesterson, A. E.; Wilde, J. H.; Qureshi, Z.; Kundu, B.; Simons, M. P.; Neumann, K. D. Imaging Diverse Pathogenic Bacteria In Vivo with 18F-Fluoromannitol PET. *J. Nucl. Med.* **2023**, *64* (5), 809−815.

(22) Ordonez, A. A.; Wintaco, L. M.; Mota, F.; Restrepo, A. F.; Ruiz-Bedoya, C. A.; Reyes, C. F.; Uribe, L. G.; Abhishek, S.; D'Alessio, F. R.; Holt, D. P.; Dannals, R. F.; Rowe, S. P.; Castillo, V. R.; Pomper, M. G.; Granados, U.; Jain, S. K. Imaging Enterobacterales Infections in Patients Using Pathogen-Specific Positron Emission Tomography. *Sci. Transl. Med.* **2021**, *13*(589), DOI: 10.1126/scitranslmed.abe9805.

(23) Mota, F.; De Jesus, P.; Jain, S. K. Kit-Based Synthesis of 2-Deoxy-2-[18F]-Fluoro-D-Sorbitol for Bacterial Imaging. *Nat. Protoc.* **2021**, *16* (11), 5274−5286.

(24) Dumont, R. A.; Keen, N. N.; Bloomer, C. W.; Schwartz, B. S.; Talbott, J.; Clark, A. J.; Wilson, D. M.; Chin, C. T. Clinical Utility of Diffusion-Weighted Imaging in Spinal Infections. *Clin. Neuroradiol.* **2019**, *29* (3), 515−522.

(25) Chenoweth, C. E.; Bassin, B. S.; Mack, M. R.; Oppenlander, M. E.; Patel, R. D.; Quint, D. J.; Seagull, F. J. *Vertebral Osteomyelitis, Discitis, and Spinal Epidural Abscess in Adults*; Michigan Medicine Clinical Care Guidelines; Michigan Medicine University of Michigan: Ann Arbor, MI, 2018.

(26) Cole, E. L.; Stewart, M. N.; Littich, R.; Hoareau, R.; Scott, P. J. H. Radiosyntheses Using Fluorine-18: The Art and Science of Late Stage Fluorination. *Curr. Top. Med. Chem.* **2014**, *14* (7), 875−900.

(27) Nakai, H.; Hachem, M. A.; Petersen, B. O.; Westphal, Y.; Mannerstedt, K.; Baumann, M. J.; Dilokpimol, A.; Schols, H. A.; Duus, J. Ø.; Svensson, B. Efficient Chemoenzymatic Oligosaccharide Synthesis by Reverse Phosphorolysis Using Cellobiose Phosphorylase and Cellodextrin Phosphorylase from Clostridium Thermocellum. *Biochimie* **2010**, *92* (12), 1818−1826.

(28) Sun, S.; You, C. Disaccharide Phosphorylases: Structure, Catalytic Mechanisms and Directed Evolution. *Synthetic and Systems Biotechnology* **2021**, *6* (1), 23−31.

(29) Luley-Goedl, C.; Nidetzky, B. Carbohydrate Synthesis by Disaccharide Phosphorylases: Reactions, Catalytic Mechanisms and Application in the Glycosciences. *Biotechnol. J.* **2010**, *5* (12), 1324−1338.

(30) O'Neill, E. C.; Field, R. A. Enzymatic Synthesis Using Glycoside Phosphorylases. *Carbohydr. Res.* **2015**, *403*, 23−37.

(31) Aisaka, K.; Masuda-Kato, T.; Chikamune, T.; Kamitori, K.; Uosaki, Y.; Saito, Y. Enzymatic Synthesis of Novel Disaccharides Using Disaccharide Phosphorylases. *J. Biosci. Bioeng.* **2000**, *90* (2), 208−213.

(32) Boos, W.; Shuman, H. Maltose/Maltodextrin System of Escherichia Coli: Transport, Metabolism, and Regulation. *Microbiol. Mol. Biol. Rev.* **1998**, *62* (1), 204−229.

(33) Dahl, M. K.; Manson, M. D. Interspecific Reconstitution of Maltose Transport and Chemotaxis in Escherichia Coli with Maltose-Binding Protein from Various Enteric Bacteria. *J. Bacteriol.* **1985**, *164* (3), 1057−1063.

(34) Gopal, S.; Berg, D.; Hagen, N.; Schriefer, E.-M.; Stoll, R.; Goebel, W.; Kreft, J. Maltose and Maltodextrin Utilization by Listeria Monocytogenes Depend on an Inducible ABC Transporter Which Is Repressed by Glucose. *PLoS One* **2010**, *5* (4), No. e10349.

(35) Ning, X.; Lee, S.; Wang, Z.; Kim, D.; Stubblefield, B.; Gilbert, E.; Murthy, N. Maltodextrin-Based Imaging Probes Detect Bacteria in Vivo with High Sensitivity and Specificity. *Nat. Mater.* **2011**, *10* (8), 602−607.

(36) Ning, X.; Seo, W.; Lee, S.; Takemiya, K.; Rafi, M.; Feng, X.; Weiss, D.; Wang, X.; Williams, L.; Camp, V. M.; Eugene, M.; Taylor, W. R.; Goodman, M.; Murthy, N. PET Imaging of Bacterial Infections with Fluorine-18-Labeled Maltohexaose. *Angew. Chem. Int. Ed* 2014, 53 (51), 14096−14101.

(37) Namavari, M.; Gowrishankar, G.; Hoehne, A.; Jouannot, E.; Gambhir, S. S. Synthesis of [18F]-Labelled Maltose Derivatives as PET Tracers for Imaging Bacterial Infection. *Mol. Imaging Biol.* 2015, 17 (2), 168−176.

(38) Gowrishankar, G.; Hardy, J.; Wardak, M.; Namavari, M.; Reeves, R. E.; Neofytou, E.; Srinivasan, A.; Wu, J. C.; Contag, C. H.; Gambhir, S. S. Specific Imaging of Bacterial Infection Using 6″-18F-Fluoromaltotriose: A Second-Generation PET Tracer Targeting the Maltodextrin Transporter in Bacteria. *J. Nucl. Med.* 2017, 58 (10), 1679−1684.

(39) Selinger, Z.; Schramm, M. Enzymatic Synthesis of the Maltose Analogues, Glucosyl Glucosamine, Glucosyl N-Acetyl-Glucosamine and Glucosyl 2-Deoxyglucose by an Extract of Neisseria Perflava. *J. Biol. Chem.* 1961, 236, 2183−2185.

(40) Putman, E. W.; Litt, C. F.; Hassid, W. Z. The Structure of D-Glucosyl-D-Xylose Synthesized by Maltose Phosphorylase1. *J. Am. Chem. Soc.* 1955, 77, 4351.

(41) Kino, K.; Shimizu, Y.; Kuratsu, S.; Kirimura, K. Enzymatic Synthesis of Alpha-Anomer-Selective D-Glucosides Using Maltose Phosphorylase. *Biosci. Biotechnol. Biochem.* 2007, 71 (6), 1598−1600.

(42) Nakai, H.; Dilokpimol, A.; Abou Hachem, M.; Svensson, B. Efficient One-Pot Enzymatic Synthesis of Alpha-(1->4)-Glucosidic Disaccharides through a Coupled Reaction Catalysed by Lactobacillus Acidophilus NCFM Maltose Phosphorylase. *Carbohydr. Res.* 2010, 345 (8), 1061−1064.

(43) Gao, Y.; Saburi, W.; Taguchi, Y.; Mori, H. Biochemical Characteristics of Maltose Phosphorylase MalE from Bacillus Sp. AHU2001 and Chemoenzymatic Synthesis of Oligosaccharides by the Enzyme. *Biosci. Biotechnol. Biochem.* 2019, 83 (11), 2097−2109.

(44) Thanna, S.; Sucheck, S. J. Targeting the Trehalose Utilization Pathways of Mycobacterium Tuberculosis. *Medchemcomm* 2016, 7 (1), 69−85.

(45) Peña-Zalbidea, S.; Huang, A. Y.-T.; Kavunja, H. W.; Salinas, B.; Desco, M.; Drake, C.; Woodruff, P. J.; Vaquero, J. J.; Swarts, B. M. Chemoenzymatic Radiosynthesis of 2-Deoxy-2-[18F]Fluoro-d-Trehalose ([18F]-2-FDTre): A PET Radioprobe for in Vivo Tracing of Trehalose Metabolism. *Carbohydr. Res.* 2019, 472, 16−22.

(46) Kalera, K.; Stothard, A. I.; Woodruff, P. J.; Swarts, B. M. The Role of Chemoenzymatic Synthesis in Advancing Trehalose Analogues as Tools for Combatting Bacterial Pathogens. *Chem. Commun.* 2020, 56 (78), 11528−11547.

(47) Elbein, A. D.; Pan, Y. T.; Pastuszak, I.; Carroll, D. New Insights on Trehalose: A Multifunctional Molecule. *Glycobiology* 2003, 13 (4), 17R−27R.

(48) Garcia-Rubio, R.; de Oliveira, H. C.; Rivera, J.; Trevijano-Contador, N. The Fungal Cell Wall: Candida, Cryptococcus, and Aspergillus Species. *Front. Microbiol.* 2020, 10, 2993.

(49) Lin, H.; Zhao, J.; Zhang, Q.; Cui, S.; Fan, Z.; Chen, H.; Tian, C. Identification and Characterization of a Cellodextrin Transporter in Aspergillus Niger. *Front. Microbiol.* 2020, 11, 145.

(50) Ruiz-Herrera, J.; Ortiz-Castellanos, L. Cell Wall Glucans of Fungi. A Review. *Cell Surf.* 2019, 5, No. 100022.

(51) Lamoth, F.; Akan, H.; Andes, D.; Cruciani, M.; Marchetti, O.; Ostrosky-Zeichner, L.; Racil, Z.; Clancy, C. J. Assessment of the Role of 1,3-β-d-Glucan Testing for the Diagnosis of Invasive Fungal Infections in Adults. *Clin. Infect. Dis.* 2021, 72 (Suppl 2), S102−S108.

(52) Axer, A.; Hermann, S.; Kehr, G.; Clases, D.; Karst, U.; Fischer-Riepe, L.; Roth, J.; Fobker, M.; Schäfers, M.; Gilmour, R.; Faust, A. Harnessing the Maltodextrin Transport Mechanism for Targeted Bacterial Imaging: Structural Requirements for Improved in Vivo Stability in Tracer Design. *ChemMedChem.* 2018, 13 (3), 241−250.

(53) Pickett, J. E.; Thompson, J. M.; Sadowska, A.; Tkaczyk, C.; Sellman, B. R.; Minola, A.; Corti, D.; Lanzavecchia, A.; Miller, L. S.; Thorek, D. L. Molecularly Specific Detection of Bacterial Lipoteichoic

Acid for Diagnosis of Prosthetic Joint Infection of the Bone. *Bone Res.* 2018, 6, 13.

(54) Hodoniczky, J.; Morris, C. A.; Rae, A. L. Oral and Intestinal Digestion of Oligosaccharides as Potential Sweeteners: A Systematic Evaluation. *Food Chem.* 2012, 132 (4), 1951−1958.

(55) Garcia, C. A.; Gardner, J. G. Bacterial α-Diglucoside Metabolism: Perspectives and Potential for Biotechnology and Biomedicine. *Appl. Microbiol. Biotechnol.* 2021, 105 (10), 4033−4052.

(56) Murosaki, S.; Muroyama, K.; Yamamoto, Y.; Kusaka, H.; Liu, T.; Yoshikai, Y. Immunopotentiating Activity of Nigerooligosaccharides for the T Helper 1-like Immune Response in Mice. *Biosci. Biotechnol. Biochem.* 1999, 63 (2), 373−378.

(57) Nihira, T.; Nakai, H.; Chiku, K.; Kitaoka, M. Discovery of Nigerose Phosphorylase from Clostridium Phytofermentans. *Appl. Microbiol. Biotechnol.* 2012, 93 (4), 1513−1522.

(58) Nihira, T.; Miyajima, F.; Chiku, K.; Nishimoto, M.; Kitaoka, M.; Ohtsubo, K.; Nakai, H. One Pot Enzymatic Production of Nigerose from Common Sugar Resources Employing Nigerose Phosphorylase. *Journal of Applied Glycoscience* 2014, 61 (3), 75−80.

(59) Kraus, M.; Görl, J.; Timm, M.; Seibel, J. Synthesis of the Rare Disaccharide Nigerose by Structure-Based Design of a Phosphorylase Mutant with Altered Regioselectivity. *Chem. Commun.* 2016, 52 (25), 4625−4627.

(60) Franceus, J.; Dhaene, S.; Decadt, H.; Vandepitte, J.; Caroen, J.; Van der Eycken, J.; Beerens, K.; Desmet, T. Rational Design of an Improved Transglucosylase for Production of the Rare Sugar Nigerose. *Chem. Commun.* 2019, 55 (31), 4531−4533.

(61) Gowrishankar, G.; Namavari, M.; Jouannot, E. B.; Hoehne, A.; Reeves, R.; Hardy, J.; Gambhir, S. S. Investigation of 6-[18F]-Fluoromaltose as a Novel PET Tracer for Imaging Bacterial Infection. *PLoS One* 2014, 9 (9), No. e107951.

(62) Namavari, M.; Gowrishankar, G.; Srinivasan, A.; Gambhir, S. S.; Haywood, T.; Beinat, C. A Novel Synthesis of 6″-[18F]-Fluoromaltotriose as a PET Tracer for Imaging Bacterial Infection. *J. Labelled Comp. Radiopharm.* 2018, 61 (5), 408−414.